remote sensing

MDPI

Article

Quantifying the Severity of Phytophthora Root Rot Disease in Avocado Trees Using Image Analysis

Arachchige Surantha Ashan Salgadoe [1,*], Andrew James Robson [1,*], David William Lamb [1], Elizabeth Kathryn Dann [2] and Christopher Searle [3]

1 Precision Agriculture Research Group (PARG), University of New England, Armidale, NSW 2351, Australia; dlamb@une.edu.au
2 Queensland Alliance for Agriculture and Food Innovation (QAAFI), University of Queensland, Brisbane, QLD 4001, Australia; e.dann@uq.edu.au
3 Stahmann Farms, McDougall Street., Toowoomba, QLD 4350, Australia; c.w.searle@bigpond.com
* Correspondence: asalgado@myune.edu.au (A.S.A.S.); arobson7@une.edu.au (A.J.R.); Tel.: +61-451-506-073 (A.S.A.S.); +61-267-734-085 (A.J.R.)

Received: 28 November 2017; Accepted: 26 January 2018; Published: 1 February 2018

Abstract: Phytophthora root rot (PRR) infects the roots of avocado trees, resulting in reduced uptake of water and nutrients, canopy decline, defoliation, and, eventually, tree mortality. Typically, the severity of PRR disease (proportion of canopy decline) is assessed by visually comparing the canopy health of infected trees to a standardised set of photographs and a corresponding disease rating. Although this visual method provides some indication of the spatial variability of PRR disease across orchards, the accuracy and repeatability of the ranking is influenced by the experience of the assessor, the visibility of tree canopies, and the timing of the assessment. This study evaluates two image analysis methods that may serve as surrogates to the visual assessment of canopy decline in large avocado orchards. A smartphone camera was used to collect red, green, and blue (RGB) colour images of individual trees with varying degrees of canopy decline, with the digital photographs then analysed to derive a canopy porosity percentage using a combination of 'Canny edge detection' and 'Otsu's' methods. Coinciding with the on-ground measure of canopy porosity, the canopy reflectance characteristics of the sampled trees measured by high resolution Worldview-3 (WV-3) satellite imagery was also correlated against the observed disease severity rankings. Canopy porosity values (ranging from 20–70%) derived from RGB images were found to be significantly different for most disease rankings ($p < 0.05$) and correlated well ($R^2 = 0.89$) with the differentiation of three disease severity levels identified to be optimal. From the WV-3 imagery, a multivariate stepwise regression of 18 structural and pigment-based vegetation indices found the simplified ratio vegetation index (SRVI) to be strongly correlated ($R^2 = 0.96$) with the disease rankings of PRR disease severity, with the differentiation of four levels of severity found to be optimal.

Keywords: avocado; canopy porosity; RGB image gap analysis; phytophthora root rot disease (PRR); vegetation indices worldview-3; multispectral satellite imagery

1. Introduction

Phytophthora root rot disease (PRR) is considered a major threat to avocado production globally [1]. In 1989, a high incidence of PRR in California resulted in a loss of US$40 million, whilst in Australia a high incidence in 1974 resulted in a 50% loss in productivity [2,3].

The soil-borne oomycete Phytophthora cinnamomi survives as thick-walled chlamydospores, which are produced in decaying roots. Under favourable conditions (warm and briefly saturated soil), sporangia are formed, from which motile zoospores are released. Zoospores are typically attracted to tips or branches of feeder roots, where they encyst and produce germ tubes that penetrate the root

cells. Mycelia grows extensively throughout the root within 72 h, and eventually feeder roots become black and brittle and die. Water and nutrient uptake is reduced, resulting in plant stress. The canopy health declines, producing small and pale green leaves at branch extremities at the top of the canopy followed by shoot die-back while other parts of the canopy remain vigorous and green. Fruit produced by infected trees is usually smaller in size and abnormal in shape [1,4].

Avocado trees affected by PRR will exhibit a visual decline in canopy condition as a result of root loss. Once identified, growers have the opportunity to implement remedial strategies to arrest further decline. These may include the addition of mulch to improve soil health or modified irrigation and phosphonate application scheduling. Currently, the commercially accepted method for estimating PRR severity in canopies in large-scale orchards is a visual estimation by trained agronomists [5] (Personal Communication with Chad Simpson, 26 May 2016—Agronomist, Simpson Farms, Childers, QLD, Australia). A visual assessment of canopy health is conducted using a standardised ranking protocol such as the 'Ciba-Geigy' reference, which provides a qualitative measurement for PRR [6]. A healthy looking tree is ranked '1', and a completely denuded tree is ranked '10', with the intermediate stages of canopy decline ranked accordingly (Table 1 and Figure 1). This ranking method, first introduced in South Africa, is the most commonly accepted and adopted method for assessing PRR disease in large orchards. In some instances, the '10 scale' rating system has been simplified to include a reduced number of classes. Simpson Farms Pty Ltd. (presently the largest avocado producer in Australia) has developed a modified version of the Ciba-Geigy scale, with only four levels of rankings instead of ten (Table 1) (personal communication with Chad Simpson, 26 May 2016—Agronomist, Simpson Farms, Childers, QLD, Australia). Horner & Jensen [7] assessed six ranking levels (healthy—'1'; denuded—'6') in an experiment to evaluate avocado plant performance over treatment effect with time.

Table 1. Ciba-Geigy and Simpson ranks used for visual estimation of Phytophthora root rot (PRR) disease severity (proportion of canopy decline).

	PRR Disease Ranking	
Visual Interpretation of Canopy	**Ciba-Geigy**	**Simpson**
Very healthy no decline	1 or 0	1
Healthy no decline	2	1
Early decline	3	1
Early decline to Moderate	4	2
Moderate decline	5	3
Moderate to severe decline	6	3
Severe decline	7	4
Very severe decline	8	4
Almost denuded	9	-
Complete denuded	10	-

Although the technique of visual tree health ranking by the human eye is accepted as common practice, it is inefficient both in terms of labour and cost requirements. Visual assessments also require a trained expert to ensure observations are comparable across orchards and across growing seasons. Mahlein [8] asserts that such methods "demand experienced individuals with well-developed skills in diagnosis and disease detection and are thus subject to human bias". The results of any assessment will vary according to an individual's experience. Furthermore, Mahlein [8] argues that the decision can be affected by temporal variation, as well as those incurred from different assessors [8–11]. An objective technique to assess PRR disease severity in tree canopies is highly desirable.

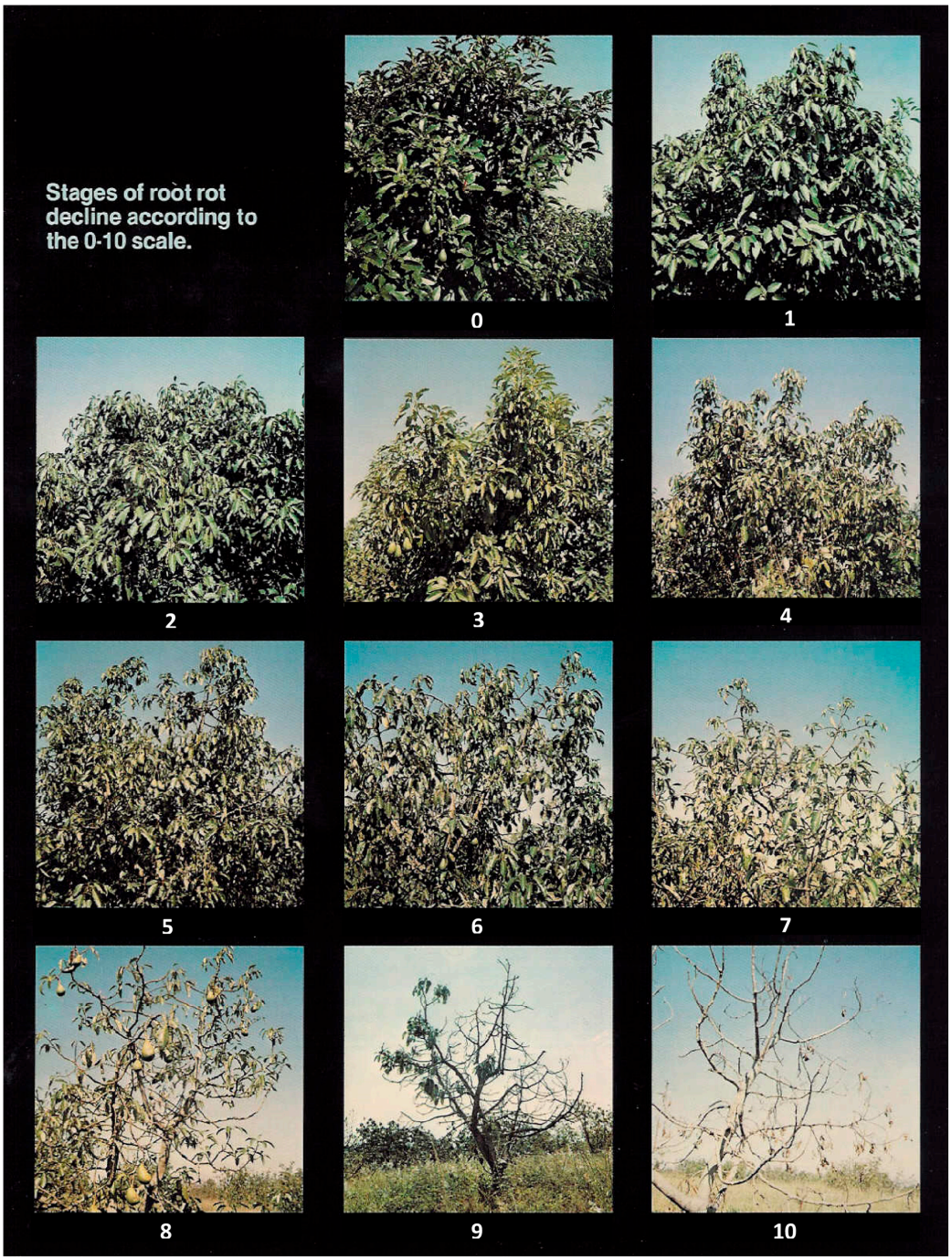

Figure 1. Ciba-Geigy Phytophthora root rot disease severity ranks (or canopy decline ranks) [6]. 0 & 1—Very healthy (no decline), 2—Healthy (no decline), 3—Early decline, 4—Early decline to moderate decline, 5—Moderate decline, 6—Moderate to severe decline, 7—Severe decline, 8—Very severe decline, 9—Almost denuded, 10—Complete denuded.

Remotely sensed digital imagery and associated computer vision and image analysis techniques presents an alternative to human vision [12]. Red, green, blue (RGB) photographs acquired by digital cameras have been successfully used to estimate canopy density, tree architecture, and growth in forest trees and grapevines [13–16]. Canopy porosity (crown porosity) or gap distribution was calculated from the proportion of sky area visible within the canopy extent [14,17–19]. It is hypothesized that this method of measuring gap distribution may present an accurate method for quantifying canopy decline

as the result of the PRR disease. To date, there has been no reported investigation of imaging/image analysis techniques for quantifying decline due to PRR disease in avocado trees.

Advanced remote sensing technologies such as multispectral and hyperspectral satellite imagery have also been demonstrated as an effective tool for detecting the presence and spatial distribution of several crop diseases including soybean root rot, Rhizoctonia blight in grass, red leaf blotch in almond trees, orange rust disease in sugarcane, and aflatoxin in peanuts [20–23]. Vegetation indices (VI) calculated from the reflectance spectra from tree canopies have been proven to be closely related to canopy morphology and leaf pigments [22,24]. VIs based on two wavebands such as simple ratio vegetation index (SRVI = NIR/Red) and normalized difference vegetation index (NDVI = [NIR − Red]/[NIR + Red]) have been shown to be sensitive to changes in overall plant condition (health/vigour), leaf area index, and canopy architecture [25]. The challenge of incorporating such VIs in distinguishing PRR is that the sensed reflectance may be influenced by other factors such as incomplete canopy cover, leaf angle, reflectance from understory vegetation, plant stress (drought or nutrient), and soil reflectance [26–28]. However, on confirmation of consistency of these other factors throughout the orchard, PRR can be a dominate driver and hence be detectable. As such, the occurrence of PRR in avocado may also be spectrally discriminated, potentially at a level of sensitivity comparable to that of the Ciba-Geigy rankings.

This paper investigates the applicability of remotely sensed imagery collected on ground with a simple mobile phone camera, as well as over the crop with high spatial resolution satellite imagery, for quantifying canopy decline associated with PRR in commercial avocado trees.

2. Materials and Methods

2.1. Tree Sampling

For this study, trees expressing different levels of tree decline attributed to PRR were selected from an avocado orchard (blocks of variety Hass and all trees at the same maturity period) at Simpson Farms Pty. Ltd. located near Childers (Bundaberg region), Queensland, Australia, (24°51′0′′S, 152°21′0′′E). Root samples collected from each tree confirmed the presence of PRR. Trees expressing the highest level of decline were predominantly located along the eastern and western portion of the blocks (Figure 4). Each sampled tree was labelled and ranked for PRR decline with visual assessment by agronomists using both Ciba-Geigy and Simpson tree health rankings (Table 1). A total of 80 trees were identified for subsequent sampling from three avocado blocks. Although it is possible that a number of biotic or abiotic constraints may contribute to the tree decline observed in the selected sample trees, experienced agronomists on location confirmed that the most likely driver of tree stress was PRR. This was further supported by the confirmed PRR observed in the collected root samples subjected to laboratory assessment.

2.2. Protocol for Ground Image Acquisition

Colour (RGB) digital images of each tree canopy were acquired using a FLIR ONE camera (FLIR Systems, OR, USA) attached to a smartphone. With a focal length f = 15 cm, a 12 μm × 12 μm element size, and a 320 × 240 pixel array, the target-camera distance of 4 m was used to produce an effective image resolution of 1.2 cm (as verified using a reference check board). Colour images were extracted in JPEG format.

For each of the selected trees, images were acquired facing the shaded side to avoid sun glare and specular reflection from the leaf surfaces. The camera azimuth was directed to avoid the sun disk either in the background or in the direct line of sight. An angle of 45° above the horizontal was also adopted for each image capture to ensure only clear sky (no sun disk) was in the background of each image, and not the canopies of trees in rows behind the selected target trees. For those trees that were significantly shorter, the capture angle was reduced accordingly so that all images included the top

most section of the canopy and a region of sky. All images were taken during daylight from 0700 h to 1600 h.

Although there are number of established imaging software programs available for extracting canopy characteristics (foliar cover and leaf area index), such as CANEYE V6 [29] (available at: https://www6.paca.inra.fr/can-eye/) and WinSCANOPY [30], these software programs were identified to be time consuming in processing and lacked the utility for customising the analysis [31]. These software programs required images to be acquired with a fish eye or classic optical lens camera (not compatible with images acquired from a smartphone) [31]. Therefore, a simple image processing technique was developed to automate gap analysis from smartphone imagery.

2.3. RGB Image Analysis

Image processing was undertaken using the MATLAB 9.2 software (The MathWorks Inc., Natick, MA, USA), using several inbuilt functions from the image processing toolbox. The method developed specifically for avocado canopies was evolved from similar analysis calculating the leaf area index (LAI) of grapevine canopies [18,32] and *Eucalyptus* [31]. The predominant processing steps included segmentation of canopy from sky and image gap analysis (sky/leaf ratio) following methodologies described by Poblete-Echeverría et al. [16] and Fuentes et al. [31].

2.3.1. Image Segmentation

In order to undertake the gap analysis, a segmented binary image was required (canopy coded as 1 and sky area coded as 0). A 10% buffered area was removed from the border of each original image to prevent the inclusion of adjacent canopies. After the cropping, the RGB image (Figure 2a) was converted to an 8-bit inverse grey-scale image (Figure 2b) with digital number (DN) values rendered according to Equation (1). Conversion of the image into grayscale inverse was effective for thresholding dark canopy area (Figure 2a) from sky (results not shown).

$$\mathrm{DN(Greyscale\ inverse)} = 255 - \left(\frac{\mathrm{DN(Red)} + \mathrm{DN(Green)} + \mathrm{DN(Blue)}}{3} \right) \quad (1)$$

The developed MATLAB script combined the outputs of the Otsu's method for thresholding histogram (Figure 2c) and Canny edge detection (Figure 2d) to generate a segmented image (Figure 3a). The Canny edge detection automatically identifies the outlines of a feature that is an advantage over identifying mixed (edge) pixels [33]. Otsu's method of thresholding the histogram automatically selects a minima value between peaks from sky and foliage [34]. Canny edge detection was able to differentiate tree canopies from sky. Image segmentation was completely automated and did not require user inputs.

The advantage of this method for segmenting sky and vegetation area is that it does not require green leaves/canopies. In comparison, CANEYE software requires mostly green leaves, as it uses a combination of red, green, and blue channel for colour thresholding leaves/canopies [29]. Also, the new method addresses a number of limitations associated with hemispheric photographs such as then need for image editing enhancement, difficulty in distinguishing foliage from canopy openings, and need for an evenness of cloud cover [35].

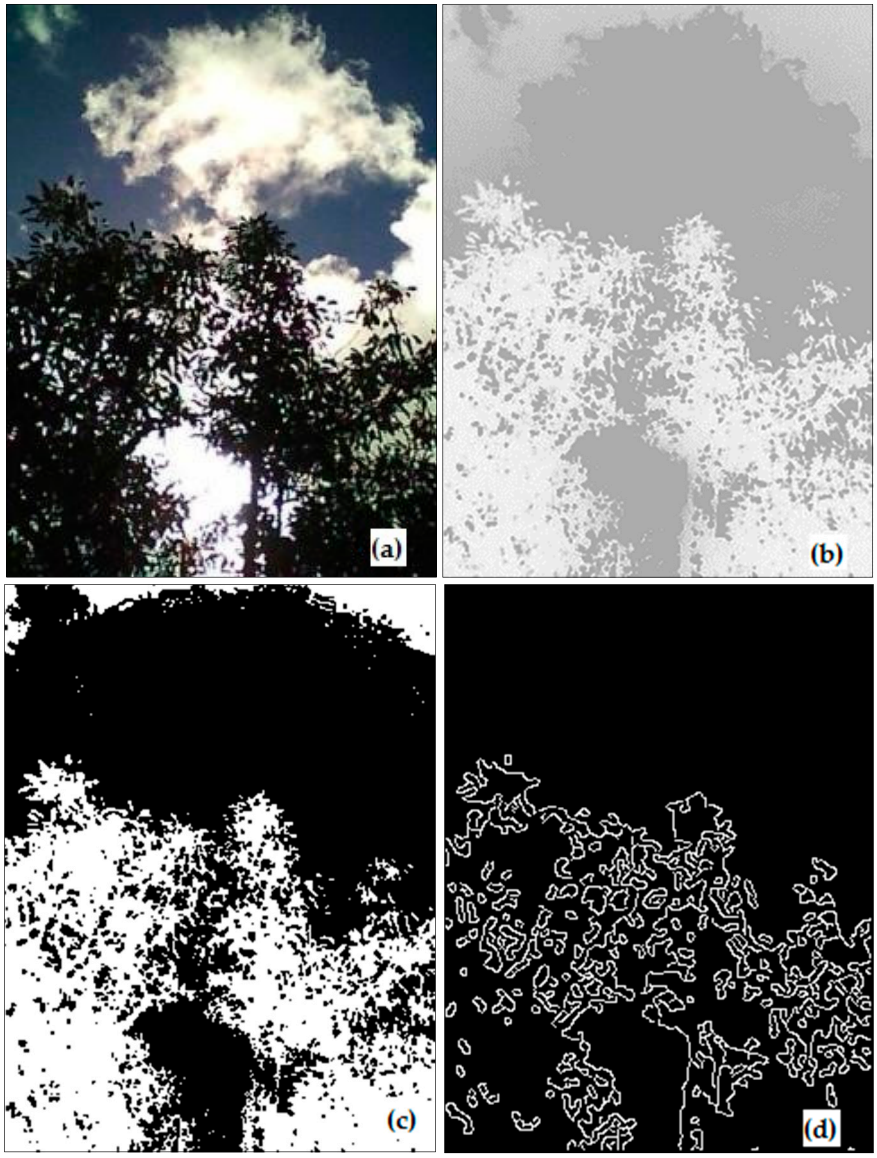

Figure 2. Example for stages during image analysis; (**a**) original image (RGB), (**b**) mono-colour image by inversing, (**c**) colour segmented by Otsu's, and (**d**) edge detection by Canny method.

2.3.2. Image Gap Analysis

Each segmented image was divided into *r* rows and *c* columns to generate n-sub-images as shown in Figure 3b. In each sub-image the total number of pixels corresponding to sky (S) and vegetation (V) (including leaves, twigs, and woody parts of the tree) were counted. If the sky to vegetation ratio (S/V) was larger than a set threshold value (*m*) for a sub-image, the corresponding sky region was classified as a 'big gap'. The sky was classified as a 'small-gap' (gS) when the S/V ratio was lower than the threshold (*m*) for a particular sub-image. The small gaps remained only within the canopy, and hence used for the porosity analysis, whereas the open sky above canopy was classified as a big gap. A sensitivity test was performed using 50 test images to select the best *r*, *c*, and *m* values to analyze gaps for the optimum calculation of canopy porosity (results not shown). The values of $m = 0.9$, $r = 11$, and $c = 4$ produced the strongest correlation between post-processed images of canopy porosity and the direct visual assessment of the porosity of the raw images.

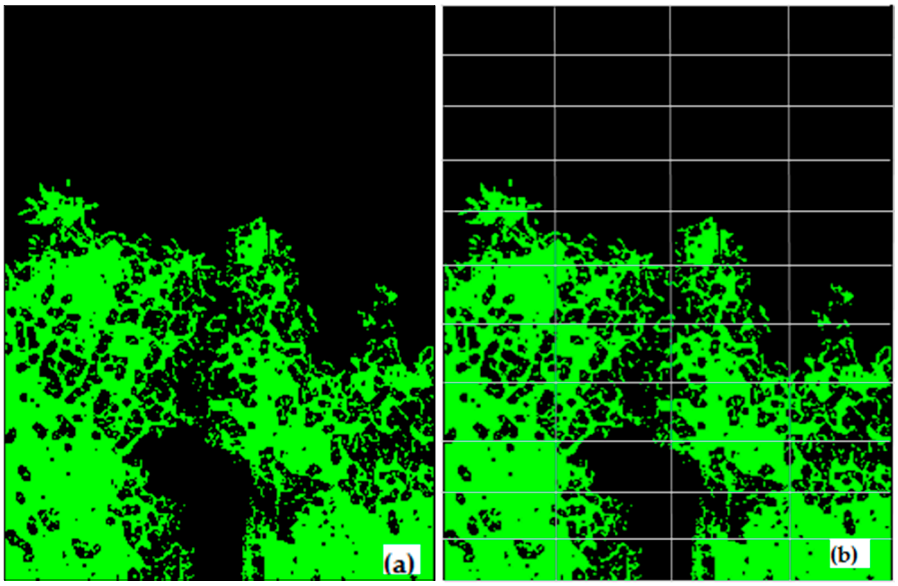

Figure 3. (**a**) Final image sky (black) and canopy area (green) segmented, and (**b**) subdivision of image into n number of sub-images for gap analysis.

2.3.3. Deriving Image Canopy Porosity

The canopy porosity (), which is the proportion of the sky area visible within the perimeter of the crowns of individual plants, was calculated using the Equation (2). The equation was modified from the original formula presented in Macfarlane et al. [14].

$$\Phi = \left\{ \frac{Tg_s}{Tg_s + T_V} \right\} \times 100\% \quad (2)$$

Here, Tg_s is the total number of small gap pixels in the complete image; T_V is the total number of vegetation pixels in the complete image.

The script took approximately 22 s to batch process 80 images automatically using an Intel Core i7 desktop computer with 3.40 GHz processing speed and 8.00 GB RAM. A percentage of porosity was derived from each input image.

2.4. Deriving Vegetation Indices from Canopy Spectral Information

The canopy radiance and reflectance information for each of the selected trees were extracted from a Worldview-3 (WV-3) satellite image (http://worldview3.digitalglobe.com/) of the orchard (Figure 4). The 1.2 m spatial resolution, 8 spectral band image was acquired on the 3rd of April, 2017 under cloudless conditions. A top-of-atmosphere correction was applied to the image prior to further analysis. To extract the canopy spectra of the sampled trees, the method of Robson et al. (2016) was used. The location of each tree, recorded with a hand-held Trimble Differential GPS (DGPS) (Trimble, Sunnyvale, CA, USA) (horizontal position error < 1 m), was overlaid onto the WV-3 image (Figure 4) in ArcGIS 10.2 (Environmental System Research Institute, Redlands, CA, USA). A 2 m radius was applied around the central crown GPS point for each tree, creating a 12.6 m^2 area of interest (AOI). Using this AOI as a mask, the 8 band WV-3 spectral information was extracted for each tree using the open source software 'Starspan GUI' (available at: https://github.com/Ecotrust/starspan). The canopy size of each sampled tree exceeded 12.6 m^2, and, as such, the derivation of a mask of this size ensured that no non-canopy specific pixels were extracted and included in the subsequent analysis. It is acknowledged, however, that in the case of severely affected trees, in which canopy decline/porosity is high, the remotely sensed imagery may be responding to a mixture of background and canopy signature. However, the background was bare soil and observed to be uniform over the site of interest

(Personal Communication with Chad Simpson, 26 May 2016—Agronomist, Simpson Farms, Childers, QLD, Australia).

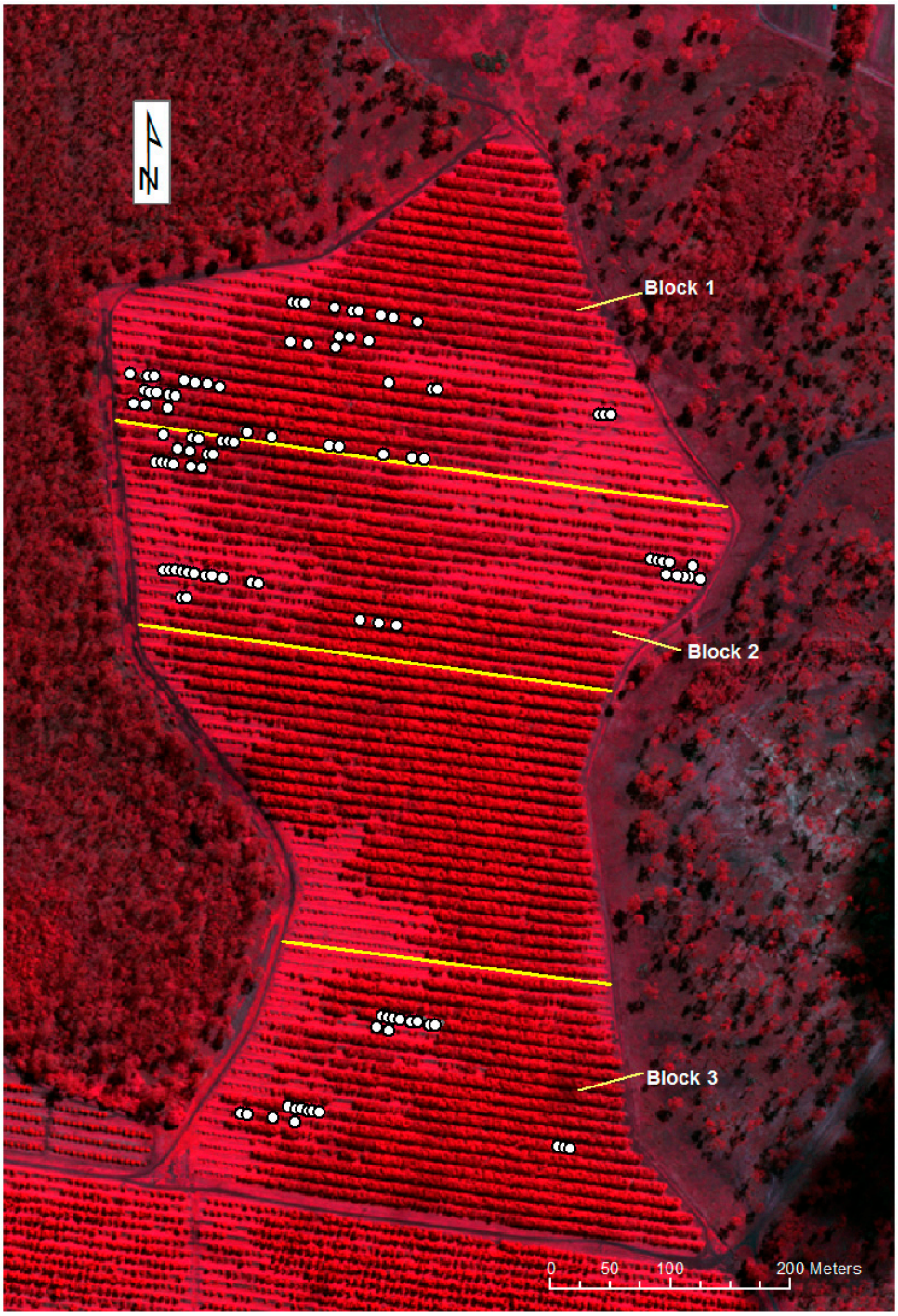

Figure 4. Worldview-3 satellite, false color image of the orchard with sample locations (acquired 3 April 2017). The location of selected trees is given as solid white circles.

To evaluate the spectral responses from the sampled trees against PRR disease severity rankings, 18 vegetation indices described in Table 2 were calculated. These indices (Table 2) were selected on the basis of having being closely related to specific features of plant leaf physiology [21,36–38].

Table 2. Vegetation indices and their formulations used in this study [24].

	Vegetation Indices	Formula *
Pigment indices		
1.	Red-edge Normalized Difference Vegetation Index	$RENDVI = (RE - R)/(RE + R)$
2.	Transformed Chlorophyll Absorption in Reflectance Index	$TCARI = 3 \times ((RE - R) - 0.2 \times (RE - G) \times (RE/R))$
3.	Structure Insensitive Pigment Index	$SIPI = (NIR1 - B)/(NIR1 + R)$
4.	Structure Insensitive Pigment Index	$CB\ SIPI = (N1R1 - CB) - (N1R1 + CB)$
5.	Normalized Difference Red-edge Index 1	$N1RENDVI = (NIR1 - RE)/(NIR1 + RE)$
6.	Normalized Difference Red-edge Index 2	$N2RENDVI = (NIR2 - RE)/(NIR2 + RE)$
Pigment and Structural indices		
7.	Normalized Difference Red-edge Index	$N1/RENDVI = (NIR1 - R)/(NIR1 + RE)$
8.	Normalized Difference NIR Index	$N1/N2\ NDVI = (NIR1 - R)/(NIR1 + NIR2)$
9.	Green normalized difference vegetation Index	$NIR1\ GNDVI = (NIR1 - G)/(NIR1 + G)$
10.	Modified Simple Ratio	$MSR = (NIR1/R - 1)/\sqrt{\left(\frac{NIR1}{R}\right) + 1}$
11.	Simple Ratio Vegetation Index	$SRVI = NIR1/R$
12.	Normalized Difference Vegetation Index 1	$N1NDVI = (NIR1 - R)/(NIR1 + R)$
13.	Normalized Difference Vegetation Index 2	$N2NDVI = (NIR2 - R)/(NIR2 + R)$
14.	Renormalized Difference Vegetation Index 1	$RDVI1 = (NIR1 - R)/\sqrt{(NIR1 + R)}$
15.	Renormalized Difference Vegetation Index 2	$RDVI2 = (NIR2 - R)/\sqrt{(NIR2 + R)}$
16.	Transformed Difference Vegetation Index 1	$TDVI1 = 1.5 \times ((NIR1 - R)/\sqrt{NIR^2 + R + 0.5})$
17.	Transformed Difference Vegetation Index 2	$TDVI2 = 1.5 \times ((NIR2 - R)/\sqrt{NIR^2 + R + 0.5})$
18.	Non Linear Index	$NLI = (NIR^2 - R)/(NIR^2 + R)$

(* Eight multispectral bands from WV-3 imagery are; coastal blue (CB): 400 nm–450 nm, blue (B): 450–510 nm, green (G): 510 nm–580 nm, yellow (Y): 585 nm–625 nm, red (R): 630 nm–690 nm, red edge (RE) 705 nm–745 nm, near-infra red 1 (NIR1): 770 nm–895 nm, near-infra red 2 (NIR2): 860 nm–1040 nm).

2.5. Statistical Analysis

The canopy porosity values derived from smartphone imagery were evaluated against the visual disease ranks catergorised from both the Ciba-Geigy and Simpson. A Chi-square 'goodness of fit' test was conducted in MATLAB 9.2 software to determine the distribution of observed values before subjecting derived canopy porosity values into parametric statistical analysis. A one-way ANOVA was initially used to test the null hypothesis that the means of derived canopy porosity for each disease rank were the same. A regression analysis was then conducted using the "Curve Fitting Toolbox" in MATLAB 9.2 to test the correlation of the derived canopy porosity values with visual ranks.

A multivariate stepwise linear regression analysis method was undertaken to determine which of the 18 VIs was best correlated to the observed visual rankings of PRR [21]. Using the "LinearModel.fit() and LinearModel.stepwise()" functions in Statistics and Machine Learning Toolbox Functions –MATLAB 9.2, the VI that most significantly correlated with the visual disease rankings was identified [36]. Although other more complex statistical methods such as partial least square regression (PLSR) have been used for identifying optimal wavelengths from hyperspectral data, Yi et al. [39] demonstrated that once the prediction model is simplified, selecting only the most significant variables (out of 19, 2-band VIs), PLSR did not perform significantly differently to stepwise regression method.

The capability of VIs to quantify PRR disease severity was compared with image-derived canopy porosity method.

3. Results

3.1. RGB Image-Derived Canopy Porosity

Visual disease rankings of the 80 selected trees ranged from '2'–'7' on the Ciba-Geigy scale and '1'–'3' on the Simpson scale. As there was only a single tree assigned into classes '1' and '8' of the Ciba-Geigy scale, these were precluded from further statistical analyses. The derived canopy porosity values exhibited a normal distribution (Chi-square test, $p < 0.05$) and ranged from 20% to 70%. There was a significant difference between the average canopy porosity for Ciba-Geigy ranks grouped according to '2–3', '4', and '5–7' (Figure 5a). Average canopy porosity was significantly different for Simpson disease rankings '1' and the combination of '2–3' (Figure 5b). A strong linear relationship

was identified between the derived canopy porosities and the Ciba-Geigy and Simpson visual disease rankings (R^2 = 0.97 and R^2 = 0.89, respectively) (Figure 5).

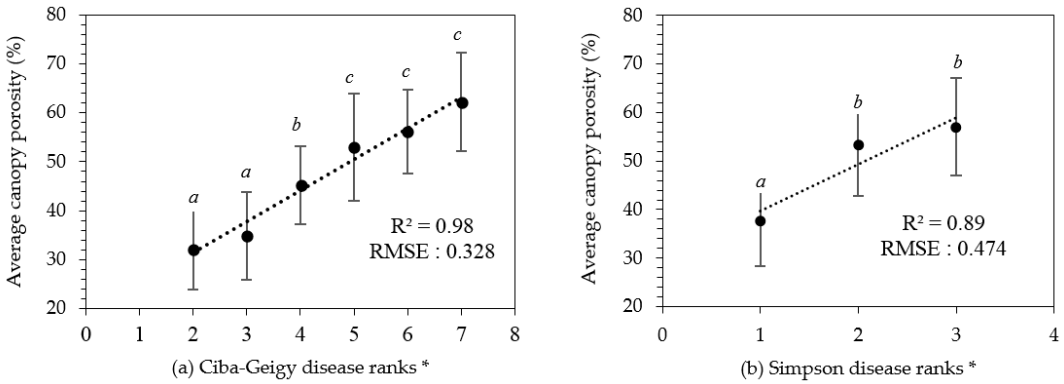

Figure 5. Results of derived canopy porosity values against disease ranks (**a**) Ciba-Geigy (**b**) Simpson. * Error bars indicate the standard deviation for each category. Averaged with similar letters are not significantly different from each other at $p < 0.05$.

3.2. Canopy Porosity Limits for Disease Ranks

Although canopy porosity values correlated strongly with both Ciba-Geigy and Simpson visual rankings, from a predictive stand-point the confident confidence limits for each of the associated mean canopy porosity values allows the Ciba-Geigy disease ranks to be re-arranged into only three ranking groups (Table 3, Figure 6). Similarly, only two groups of Simpson rankings could be predicted (result not shown). Hence, we can define three modified Ciba-Geigy ranks '1*', '2*', and '3*' with an associated confidence of 99% (Table 3).

Table 3. Confidence limits for porosity values with modified Ciba-Geigy disease ranks.

Modified Ciba-Geigy Dis. Ranks	Confidence Limits for Derived Canopy Porosity %		Original Ciba-Geigy Disease Ranks	Average Canopy Porosity % *	Standard Deviation	Confidence Level
	Lower	Upper				
1 *	29.40	38.24	2 & 3	33.82 [a]	8.404	99%
2 *	40.46	49.98	4	45.22 [b]	7.83	99%
3 *	51.70	60.06	5, 6 & 7	55.88 [c]	9.99	99%

* Denotes that are different from rank numeric of Table 1. Average canopy porosity % with superscripts (a, b and c) are significantly different from each other ($p < 0.05$).

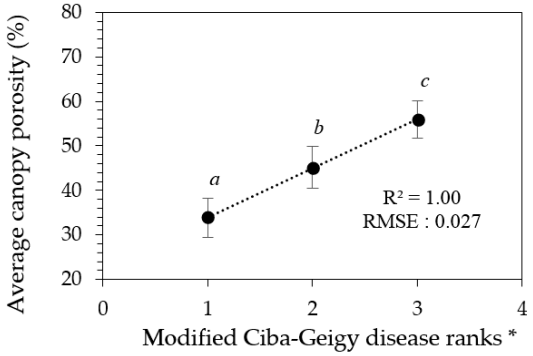

Figure 6. Graphical interpretation of confidence limits relating derived porosity values and the modified Ciba-Geigy disease ranks in Table 3. * Error bars indicate the confidence limits for each rank. Means with similar letters are not significantly different from each other at $p < 0.05$.

3.3. Remotely Sensed VI for Estimating Visual Rankings and Camera-Derived Canopy Porosity

The pigment-based, remotely sensed vegetation indices RENDVI, N1RENDVI, and N2RENDVI, and all of the leaf structure-based indices, produced statistically significant correlations with the visually allocated disease ranks and the handheld camera-derived canopy porosity (Table 4). The simple ratio vegetation index (SRVI) exhibited strongest significant correlation with both sets of disease rankings, as well as the derived canopy porosity. Therefore, SRVI was chosen as the best fit VI out of the eighteen tested. The average SRVI values for respective disease rankings were plotted in Figure 7. The data in Figure 7 also includes indicators of significance between the groupings. The remotely sensed data (from satellite) can discriminate Ciba-Geigy ranks when grouped as '2', '3–4', '5', and '6–7' (Table 5 and Figure 8), which is a greater number of groupings (4) than by the hand held smartphone camera-derived porosity method (3).

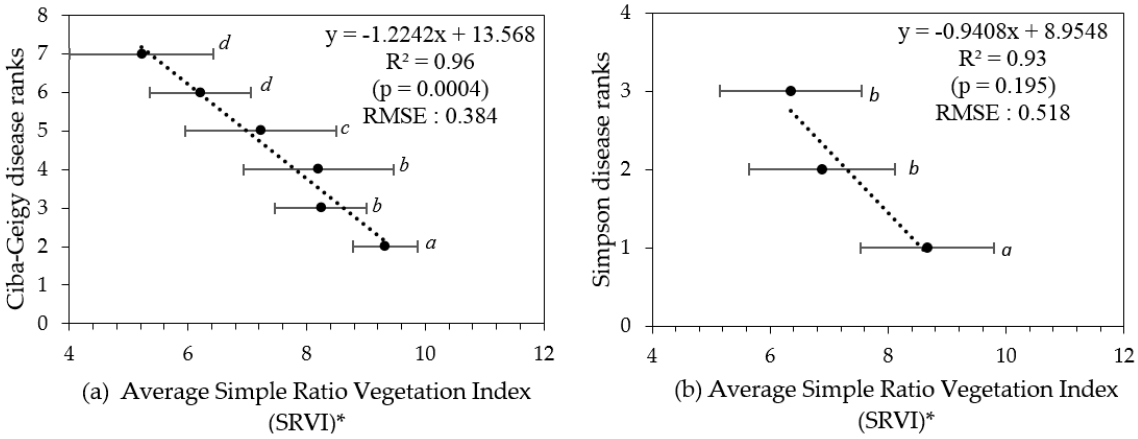

Figure 7. (**a**) Ciba-Geigy and (**b**) Simpson disease ranks versus average simple ratio vegetation index (SRVI) values (respective trees grouped into their disease ranks). * Error bars indicate the standard deviation for each category. Means with similar letters are not significantly different from each other at $p > 0.05$.

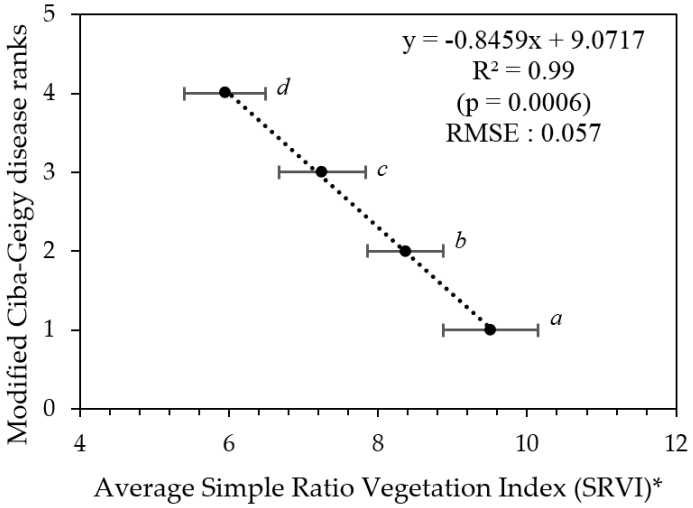

Figure 8. Modified Ciba-Geigy disease ranks as a function of average SRVI (trees grouped according to their modified Ciba-Geigy disease ranks in Table 5). * Error bars indicate the confidence limits for each rank. Means with similar letters are not significantly different from each other at $p > 0.05$.

Table 4. Significance of vegetation indices correlating with visual disease rankings and derived canopy porosity from stepwise regression analysis.

Vegetation Indices		*p*-Values for Each Correlation Combination with VI		
		Ciba-Geigy	Simpson	Derived Canopy Porosity %
Pigment indices				
1.	RENDVI	2.53×10^{-10}	3.24×10^{-8}	1.73×10^{-8}
2.	TCARI	0.86	0.947	0.789
3.	SIPI	5.17×10^{-5}	1.05×10^{-3}	3.23×10^{-5}
4.	CB SIPI	4.42×10^{-9}	3.07×10^{-7}	3.93×10^{-9}
5.	N1RENDVI	4.53×10^{-9}	9.36×10^{-8}	6.26×10^{-10}
6.	N2RENDVI	5.43×10^{-8}	2.46×10^{-7}	1.04×10^{-8}
Pigment and Structural indices				
7.	N1/RENDVI	1.68×10^{-11}	2.36×10^{-9}	2.40×10^{-11}
8.	N1/N2 NDVI	2.24×10^{-10}	4.30×10^{-9}	7.31×10^{-9}
9.	N1R1 GNDVI	2.41×10^{-12}	3.17×10^{-9}	8.97×10^{-12}
10.	MSR	1.13×10^{-12}	2.16×10^{-10}	6.96×10^{-12}
11.	SRVI *	1.09×10^{-12} *	1.51×10^{-10} *	4.50×10^{-12} *
12.	N1NDVI	5.79×10^{-12}	1.68×10^{-9}	8.21×10^{-11}
13.	N2NDVI	5.12×10^{-12}	8.19×10^{-10}	8.28×10^{-11}
14.	RDVI1	1.50×10^{-10}	8.90×10^{-9}	2.23×10^{-10}
15.	RDVI2	1.73×10^{-10}	5.50×10^{-9}	4.20×10^{-10}
16.	TDVI1	7.17×10^{-12}	2.10×10^{-9}	1.06×10^{-10}
17.	TDVI2	6.37×10^{-12}	1.04×10^{-9}	1.06×10^{-10}
18.	NLI	2.57×10^{-11}	6.52×10^{-9}	1.00×10^{-10}

* Significant VI selected by stepwise regression analysis ($p < 0.05$).

Table 5. Confidence limits for porosity values with modified Ciba-Geigy disease ranks.

Modified Ciba-Geigy Disease Ranks	Confidence Limits of SRVI		Original Ciba-Geigy Disease Ranks	Average SRVI Values	Standard Deviation	Confidence Level
	Upper	Lower				
1 **	10.15	8.87	2	9.51 [a]	0.83	97%
2 **	8.87	7.86	3 & 4	8.37 [b]	1.25	98%
3 **	7.83	6.67	5	7.25 [c]	0.93	98%
4 **	6.49	5.40	6 & 7	5.95 [d]	1.12	98%

** Denotes that are different from rank numeric of Table 3. Average SRVI values with superscripts (a, b, c and d) are significantly different from each other ($p < 0.05$).

3.4. Generating PRR Disease Severity Map from WV-3 Satellite Imagery

To produce disease severity map from the results, each pixel of WV-3 satellite imagery (Figure 4) was first converted to SRVI values using the function in Table 2, then to disease severity values using the regression formula in Figure 8 in ENVI 5.1 (https://esriaustralia.com.au/envi). Imagery was then classified into disease severity zones using SRVI confidence limit values in Table 5 in ArcGIS 10.2. The classified image was exported as a TIFF image to Google Earth (Google Earth Pro, 2017) and overlaid with the elevation model. Spatial distribution of PRR disease in the orchard was depicted in map form (Figure 9).

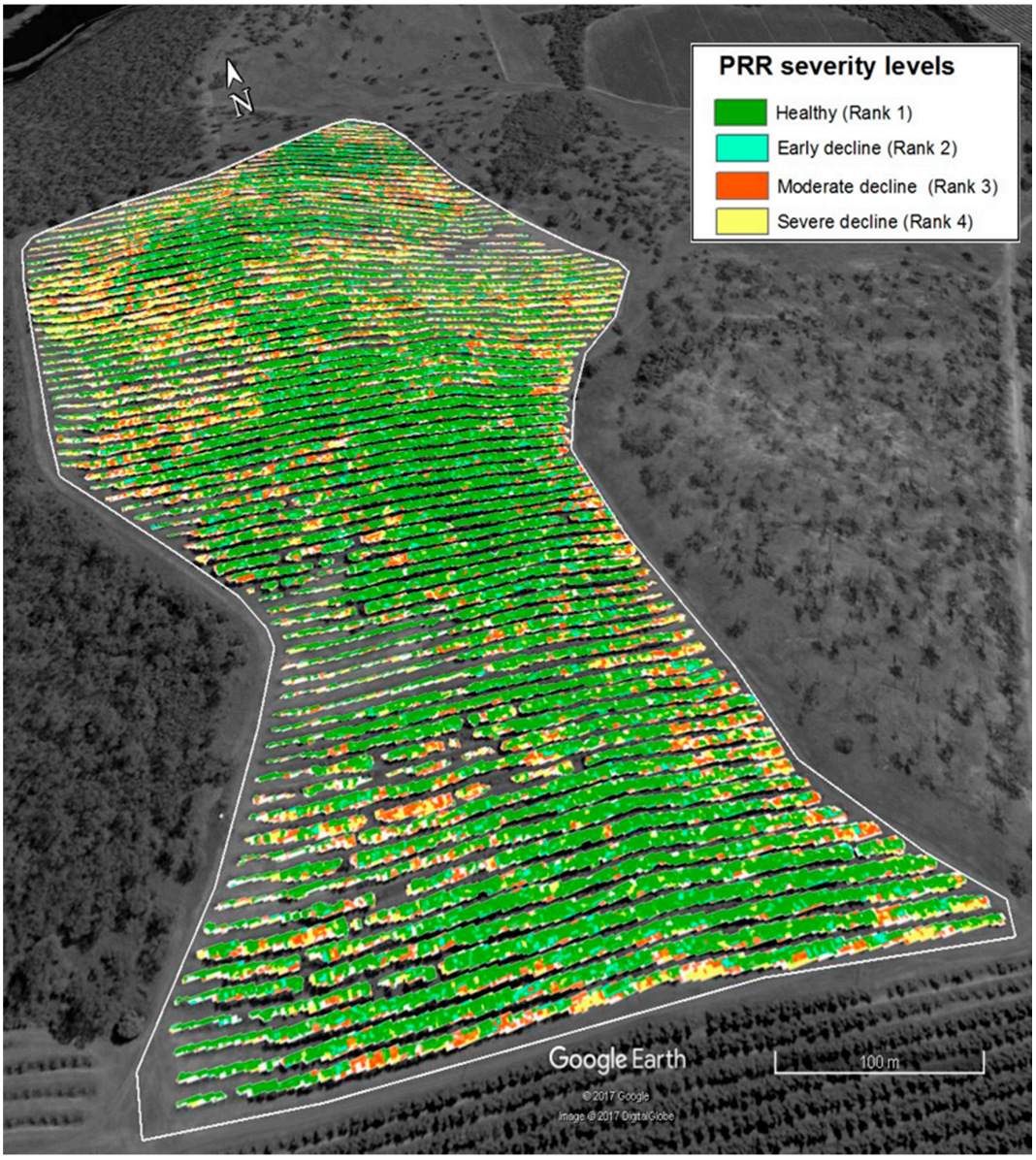

Figure 9. PRR severity distribution map of the avocado orchard classified according to SRVI and superimposed over an elevation layer.

4. Discussion

RGB images from a smartphone could be used to generate porosity values for individual trees and for the delineation of three PRR disease class groupings from the Ciba-Geigy ranks, namely a combined group of Ciba-Geigy '2' and '3', Ciba-Geigy '4', and then Ciba-Geigy-'5'–'7'. In comparison, the multispectral WV-3 satellite imagery was able to sense additional non-visible spectral information reflected from tree canopies. In both methods, grouping non-significant categories improved the correlation as well as reduced the error (RMSE). The simple ratio of NIR:Red reflectance (SRVI) was identified to be the most sensitive VI to PRR severity, especially for differentiating early decline in the trees (Ciba-Geigy-'3') from healthy trees (Ciba-Geigy-'2') (Figure 7), which was not possible to do by the RGB porosity method. It is likely that the addition of the near infrared band resulted in the increased sensitivity.

Pinter, Jr. et al. [26] identified stressed vegetation as producing lower solar reflectance in the near infrared region than healthy vegetation, especially as a result of drought stress. As the trees sampled for

this research were selected from a well-irrigated avocado orchard, it is likely that canopy decline was the result of PRR and not purely from a lack of water. Considering the level of stress, the results also explain measured amount of stress (indicated by SRVI values) increased as disease severity increase. Understanding spatial and temporal differences of the disease spreading would be very useful for disease management [40]. The derived PRR disease severity distribution map of Figure 9 illustrates the distribution of trees in severe decline at the eastern and western boundaries, which was subsequently attributed to water logging conditions in lower elevation areas. Poorly drained soil is considered a favourable condition exacerbating the development of PRR disease [41].

Although remote sensed methods (hand held smartphone imagery and satellite imagery) were able to quantify PRR severities into number of discrete groups (similar to visual estimation), requirement of a preliminary disease confirmation test prior imaging can be considered as a possible limitation. This method would not be appropriate if any other abiotic factor (insect/disease) causing canopy decline in the orchard is reported. Therefore, an orchard maintaining good agricultural practices such as irrigation and fertilization may qualify to use these methods.

The best season for adopting these proposed methods would be during spring, as PRR disease symptoms begins to show-up during this season in avocado tree canopies (Personal Communication with Chad Simpson, 26 May 2016—Agronomist, Simpson Farms, Childers, QLD, Australia). As PRR disease symptoms follow a particular pattern in progressing as shown in Figure 1, the spectral reflectance associated with the disease can be expected to be the same if the driven force for plant vigour was confirmed to be dominated by PRR. However, proposed methods need to be further tested upon different avocado tree varieties and maturity stages.

Future research work can be carried out with explicit techniques such as hyperspectral information, while additional VIs such as crop water stress index (CWSI) and photochemical reflectance index as suggested by Apan et al. [42] and R Calderón et al. [21] would serve as possible indicators for understanding physiological responses due to early PRR disease attacks. Further, advanaced statistical methods such as partial least square regression (PLSR) [43] can be adopted to imporve classification of spectral data related to PRR disease with high diamentional bands and VIs. This allows for the combination of a large set of independent variables without loosing much hyperspectral inforamtion [44,45]. Alternatively, advanced image analysis methods, such as colour feature extreme learning machines suggested by Sadgrove et al. [46], could be tested to improve the accuracy of delineating features extracted by RGB images. Both the remote sensing and smart-phone image-based results are encouraging from the perspective of application to inverted radiative transfer models [47]. The (albeit presently limited) discrimination of PRR levels may be improved by incorporating the reflectance/porosity data (at varying scales) into inverted radiative transfer models to be able to map key parameters. This will be an area of ongoing investigation.

5. Conclusions

Both RGB images acquired from hand-held cameras, and multispectral imagery from high spatial resolution satellites, can be used to indicate PRR disease severity or canopy decline in avocado orchards, ostensibly into high, medium, and low ranges. The use of satellite imagery also provides the ability to create PRR severity maps across entire orchards.

Compared to traditional methods of visual estimation, this technique suggests a possibility of using computational and remote sensing technologies for objectively and, importantly, quantitatively assessing PRR disease severities.

With further improvements for the smartphone technique, mobile applications can be introduced for assessing PRR severities in diseased avocado orchards. Further, satellite findings can be useful for advanced research work in developing future techniques for early diagnosis of PRR disease in avocado.

Acknowledgments: The authors gratefully acknowledge the Australian Federal Government 'Rural R&D for Profit' scheme and Hort Innovation Australia Horticulture Innovation for funding this Research. The authors sincerely appreciate the support provided for this research by Simpson Farms Pty. Ltd. (Childers, QLD 4660, Australia),

in particular Chad Simpson. Finally, authors would like to offer sincere gratitude to Greg Falzon—(Lecturer, Sch. of Sci. and Tech., UNE) for guiding in statistical analysis methods and M. Moshiur Rahman (PARG, UNE) for helping in producing disease severity maps.

Author Contributions: All the authors jointly conceived and designed the experiments; A.S.A.S. performed the field work with the contribution of C.W.S.; A.S.A.S. analyzed the data and lead writing of the paper with all authors making contributions.

Conflicts of Interest: The authors declare no conflict of interest.

References

1. Erwin, D.C.; Ribeiro, O.K. Phytophthora cinnamomi Rands (1922) var. cinnamomi. In *Phytophthora Diseases Worldwide*; APS Press: St. Paul, MN, USA, 1996; pp. 269–279. ISBN 978-0-89054-212-5.
2. Marais, L.J.; Menge, J.A.; Bender, G.S.; Faber, B. Phytophthora Root Rot. *AvoResearch Calif. Avocado Comm.* **2002**, *2*, 3–6.
3. Pegg, K.; Whiley, A.; Langdon, P.; Saranah, J. Comparison of phosetyl-Al, phosphorous acid and metalaxyl for the long-term control of Phytophthora root rot of avocado. *Aust. J. Exp. Agric.* **1987**, *27*, 471–474. [CrossRef]
4. Dann, E.K.; Ploetz, R.C.; Coates, L.M.; Pegg, K.G. Foliar, Fruit and Soilborne Diseases. In *The Avocado: Botany, Production and Uses*; Schaffer, B., Whiley, A.W., Wolstenholme, B.N., Eds.; CABI: Cambridge, MA, USA, 2012; pp. 397–398. ISBN 978-1-84593-701-0.
5. Nutter, F.W.; Esker, P.D.; Netto, R.A.C. Disease Assessment Concepts and the Advancements Made in Improving the Accuracy and Precision of Plant Disease Data. *Eur. J. Plant Pathol.* **2006**, *115*, 95–103. [CrossRef]
6. Darvas, J.M.; Toerien, J.C.; Mine, D.L. Control of Avocado Root Rot by Trunk Injection with Phosethyl-Al. *Plant Dis.* **1984**, *68*, 691–693. [CrossRef]
7. Horner, I.J.; Jensen, E.H. *Evaluation of Phytoptora Control in Avocados*; New Zealand Avocado Growers' Association Annual Research Report; Avocado Grower's Association: Tauranga, New Zealand, 2004; pp. 1–7.
8. Mahlein, A.-K. Plant Disease Detection by Imaging Sensors—Parallels and Specific Demands for Precision Agriculture and Plant Phenotyping. *Plant Dis.* **2016**, *100*, 241–251. [CrossRef]
9. Bock, C.H.; Parker, P.E.; Cook, A.Z.; Gottwald, T.R. Visual Rating and the Use of Image Analysis for Assessing Different Symptoms of Citrus Canker on Grapefruit Leaves. *Plant Dis.* **2008**, *92*, 530–541. [CrossRef]
10. Newton, A.C.; Hackett, C.A. Subjective components of mildew assessment on spring barley. *Eur. J. Plant Pathol.* **1994**, *100*, 395–412. [CrossRef]
11. Steddom, K.; Bredehoeft, M.W.; Khan, M.; Rush, C.M. Comparison of Visual and Multispectral Radiometric Disease Evaluations of Cercospora Leaf Spot of Sugar Beet. *Plant Dis.* **2005**, *89*, 153–158. [CrossRef]
12. Nixon, M.S.; Aguado, A.S. Human and computer vision. In *Feature Extraction and Image Processing*; Elsevier: Oxford, UK, 2008; pp. 1–29. ISBN 978-0-08-050625-8.
13. Goodenough, A.E.; Goodenough, A.S. Development of a Rapid and Precise Method of Digital Image Analysis to Quantify Canopy Density and Structural Complexity. *Int. Sch. Res. Not.* **2012**, *2012*, 1–11. [CrossRef]
14. Macfarlane, C.; Hoffman, M.; Eamus, D.; Kerp, N.; Higginson, S.; McMurtrie, R.; Adams, M. Estimation of leaf area index in eucalypt forest using digital photography. *Agric. For. Meteorol.* **2007**, *143*, 176–188. [CrossRef]
15. Mora, M.; Avila, F.; Carrasco-Benavides, M.; Maldonado, G.; Olguín-Cáceres, J.; Fuentes, S. Automated computation of leaf area index from fruit trees using improved image processing algorithms applied to canopy cover digital photograpies. *Comput. Electron. Agric.* **2016**, *123*, 195–202. [CrossRef]
16. Poblete-Echeverría, C.; Fuentes, S.; Ortega-Farias, S.; Gonzalez-Talice, J.; Yuri, J. Digital Cover Photography for Estimating Leaf Area Index (LAI) in Apple Trees Using a Variable Light Extinction Coefficient. *Sensors* **2015**, *15*, 2860–2872. [CrossRef] [PubMed]
17. Castillo-Ruiz, F.; Castro-Garcia, S.; Blanco-Roldan, G.; Sola-Guirado, R.; Gil-Ribes, J. Olive Crown Porosity Measurement Based on Radiation Transmittance: An Assessment of Pruning Effect. *Sensors* **2016**, *16*, 723. [CrossRef] [PubMed]

18. De Bei, R.; Fuentes, S.; Gilliham, M.; Tyerman, S.; Edwards, E.; Bianchini, N.; Smith, J.; Collins, C. VitiCanopy: A Free Computer App to Estimate Canopy Vigor and Porosity for Grapevine. *Sensors* **2016**, *16*, 585. [CrossRef] [PubMed]
19. Pekin, B.; Macfarlane, C. Measurement of crown cover and leaf area index using digital cover photography and its application to remote sensing. *Remote Sens.* **2009**, *1*, 1298–1320. [CrossRef]
20. Apan, A.; Held, A.; Phinn, S.; Markley, J. Detecting sugarcane 'orange rust' disease using EO-1 Hyperion hyperspectral imagery. *Int. J. Remote Sens.* **2004**, *25*, 489–498. [CrossRef]
21. Calderón, R.; Navas-Cortés, J.A.; Lucena, C.; Zarco-Tejada, P.J. High-resolution airborne hyperspectral and thermal imagery for early detection of Verticillium wilt of olive using fluorescence, temperature and narrow-band spectral indices. *Remote Sens. Environ.* **2013**, *139*, 231–245. [CrossRef]
22. Calderón, R.; Navas-Cortés, J.; Zarco-Tejada, P. Early Detection and Quantification of Verticillium Wilt in Olive Using Hyperspectral and Thermal Imagery over Large Areas. *Remote Sens.* **2015**, *7*, 5584–5610. [CrossRef]
23. Robson, A. Remote Sensing Application for the Determination of Yeild, Maturity and Aflatoxin Contamination in Peanut. Ph.D. Thesis, University of Queensland, Brisbane, Australia, 2007.
24. Robson, A.; Rahman, M.M.; Muir, J.; Saint, A.; Simpson, C.; Searle, C. Evaluating satellite remote sensing as a method for measuring yield variability in Avocado and Macadamia tree crops. *Adv. Anim. Biosci.* **2017**, *8*, 498–504. [CrossRef]
25. Jackson, R.D.; Huete, A.R. Interpreting vegetation indexes. *Prev. Vet. Med.* **1991**, *11*, 185–200. [CrossRef]
26. Pinter, P.J., Jr.; Hatfield, J.L.; Schepers, J.S.; Barnes, E.M.; Moran, M.S.; Daughtry, C.S.T.; Upchurch, D.R. Remote Sensing for Crop Management. *Photogramm. Eng. Remote Sens.* **2003**, *69*, 647–664. [CrossRef]
27. Hatfield, J.L.; Gitelson, A.A.; Schepers, J.S.; Walthall, C.L. Application of Spectral Remote Sensing for Agronomic Decisions. *Agron. J.* **2008**, *100*, 117–131. [CrossRef]
28. Barton, C.V.M. Advances in remote sensing of plant stress. *Plant Soil* **2012**, *354*, 41–44. [CrossRef]
29. Weiss, M. *Can_Eye V6.4.91 User Manual*; French National Institute for Agriculture Research (INRA): Toulouse, France, 2017.
30. Macfarlane, C.; Arndt, S.K.; Livesley, S.J.; Edgar, A.C.; White, D.A.; Adams, M.A.; Eamus, D. Estimation of leaf area index in eucalypt forest with vertical foliage, using cover and fullframe fisheye photography. *For. Ecol. Manag.* **2007**, *242*, 756–763. [CrossRef]
31. Fuentes, S.; Palmer, A.R.; Taylor, D.; Zeppel, M.; Whitley, R.; Eamus, D. An automated procedure for estimating the leaf area index (LAI) of woodland ecosystems using digital imagery, MATLAB programming and its application to an examination of the relationship between remotely sensed and field measurements of LAI. *Funct. Plant Biol.* **2008**, *35*, 1070–1079. [CrossRef]
32. Fuentes, S.; Poblete-Echeverría, C.; Ortega-Farias, S.; Tyerman, S.; De Bei, R. Automated estimation of leaf area index from grapevine canopies using cover photography, video and computational analysis methods: New automated canopy vigour monitoring tool. *Aust. J. Grape Wine Res.* **2014**, *20*, 465–473. [CrossRef]
33. Liu, H.; Jezek, K.C. Automated extraction of coastline from satellite imagery by integrating Canny edge detection and locally adaptive thresholding methods. *Int. J. Remote Sens.* **2004**, *25*, 937–958. [CrossRef]
34. Otsu, N. A Threshold Selection Method from Gray-Level Histograms. *IEEE Trans. Syst. Man Cybern.* **1979**, *9*, 62–66. [CrossRef]
35. Jonckheere, I.; Fleck, S.; Nackaerts, K.; Muys, B.; Coppin, P.; Weiss, M.; Baret, F. Review of methods for in situ leaf area index determination. *Agric. For. Meteorol.* **2004**, *121*, 19–35. [CrossRef]
36. López-López, M.; Calderón, R.; González-Dugo, V.; Zarco-Tejada, P.; Fereres, E. Early Detection and Quantification of Almond Red Leaf Blotch Using High-Resolution Hyperspectral and Thermal Imagery. *Remote Sens.* **2016**, *8*, 276. [CrossRef]
37. Mahlein, A.-K.; Oerke, E.-C.; Steiner, U.; Dehne, H.-W. Recent advances in sensing plant diseases for precision crop protection. *Eur. J. Plant Pathol.* **2012**, *133*, 197–209. [CrossRef]
38. Mahlein, A.-K.; Steiner, U.; Dehne, H.-W.; Oerke, E.-C. Spectral signatures of sugar beet leaves for the detection and differentiation of diseases. *Precis. Agric.* **2010**, *11*, 413–431. [CrossRef]
39. Yi, Q.; Jiapaer, G.; Chen, J.; Bao, A.; Wang, F. Different units of measurement of carotenoids estimation in cotton using hyperspectral indices and partial least square regression. *ISPRS J. Photogramm. Remote Sens.* **2014**, *91*, 72–84. [CrossRef]

40. Nelson, M.R.; Orum, T.V.; Jaime-Garcia, R.; Nadeem, A. Applications of Geographic Information Systems and Geostatistics in Plant Disease Epidemiology and Management. *Plant Dis.* **1999**, *83*, 308–319. [CrossRef]
41. Erwin, D.C.; Ribeiro, O.K. Phytophthora Diseases Worldwide. In *Phytophthora Diseases Worldwide*; APS Press: St. Paul, MN, USA, 1996; pp. 8–38. ISBN 978-0-89054-212-5.
42. Apan, A.; Held, A.; Phinn, S.; Markley, J. Formulation and assessment of narrow-band vegetation indices from EO-1 Hyperion imagery for discriminating sugarcane disease. In Proceedings of the Spatial Sciences Institute Biennial Conference, Canberra, Australia, 22–26 September 2003.
43. Suarez, L.A.; Apan, A.; Werth, J. Detection of phenoxy herbicide dosage in cotton crops through the analysis of hyperspectral data. *Int. J. Remote Sens.* **2017**, *38*, 6528–6553. [CrossRef]
44. Darvishzadeh, R.; Skidmore, A.; Schlerf, M.; Atzberger, C.; Corsi, F.; Cho, M. LAI and chlorophyll estimation for a heterogeneous grassland using hyperspectral measurements. *ISPRS J. Photogramm. Remote Sens.* **2008**, *63*, 409–426. [CrossRef]
45. Fu, Y.-Y.; Wang, J.-H.; Yang, G.-J.; Song, X.-Y.; Xu, X.-G.; Feng, H.-K. Band depth analysis and partial least square regression based winter wheat biomass estimation using hyperspectral measurements. *Guang Pu Xue Yu Guang Pu Fen Xi Guang Pu* **2013**, *33*, 1315–1319. [CrossRef] [PubMed]
46. Sadgrove, E.J.; Falzon, G.; Miron, D.; Lamb, D. Fast object detection in pastoral landscapes using a Colour Feature Extreme Learning Machine. *Comput. Electron. Agric.* **2017**, *139*, 204–212. [CrossRef]
47. Meroni, M.; Colombo, R.; Panigada, C. Inversion of a radiative transfer model with hyperspectral observations for LAI mapping in poplar plantations. *Remote Sens. Environ.* **2004**, *92*, 195–206. [CrossRef]